HiSST: 3rd International Conference on High-Speed Vehicle Science Technology

14–19 April 2024, Busan, Korea

Comparison of Different Fidelity Approaches for the Coupled Aerothermodynamic Heating of Hypersonic Reentry Vehicles

Fynn Barz[1] Marius Franze[2]

Abstract

In the present study the influence of different fidelity flow solvers and structure models on the aerothermodynamic heating of High Lift Reentry Vehicle (HLRV) is investigated. The study is carried out on a generic waverider (WR) geometry. The reference solution is computed by a high-fidelity unsteady RANS coupled multi-disciplinary simulation. The analysis is performed for the forced flight along a reference trajectory. The coupled calculation leads to a realistic evaluation of the overall heating for the vehicle entering the atmosphere of the Earth. The low-fidelity aerodynamic solution is calculated by the Shock-Expansion method. The aerothermodynamic heating is included by the Eckert-Reference-Enthalpy method and the Reynolds analogy. The vehicle structure is represented by a one-dimensional heat conduction solver with a simplified material model. The differences between the models of different fidelity are shown.

Keywords: *Waverider, Hypersonic Reentry, Multi-Fidelity*

Nomenclature

Abbreviations

AoA	Angle of Attack
CFD	Computational Fluid Dynamics
CoNF^{2}aS^2	Coupled Numerical Fluid Flight Mechanic and Structure Simulation
CSM	Computational Structure Mechanics
DLR	German Aerospace Center
HLRV	High Lift Reentry Vehicle
RAM	Random-Access Memory
TPS	Thermal Protection System
WR	Waverider

Latin

C_H	Heat Transfer Coefficient
M	Mach Number
Pr	Prandtl Number
R	Generating Shock Radius
Re	Reynolds Number
T	Temperature
b_H	Half Wingspan
c_f	Skin Friction Coefficient
d	Leading Edge Normal Distance
h	Altitude
$\dot{q}$	Heat Flux
r_{LE}	Leading Edge Radius
s	Reynolds Analogy Factor
t	Time of Flight
x, y, z	Coordinates

Greek

α	Angle of Attack
ε	Emissivity
θ_s	Semi-Vertical Shock Angle
λ	Thermal Conductivity
ρ	Density
σ	Stefan-Boltzmann Constant
ψ	Thickness of the Material

Superscripts

$*$	Value at Eckert-Reference Temperature

Subscripts

e	Boundary Layer Edge Value
r	Radiation Value
w	Wall Value
∞	Free Stream Value

---

[1] *German Aerospace Center (DLR), Institute of Aerodynamics and Flow Technology, Spacecraft, Lilienthalplatz 7, 38108 Braunschweig, Germany, fynn.barz@dlr.de*

[2] *German Aerospace Center (DLR), Institute of Aerodynamics and Flow Technology, Spacecraft, Lilienthalplatz 7, 38108 Braunschweig, Germany, marius.franze@dlr.de*

1. Introduction

HLRV are of increasing interest during the last years. The reason is their maneuverability and the ability to fly at high Mach numbers over a long duration of time. Hence, such configurations are not only interesting for the transportation purpose but also from a defence perspective. Furthermore, they are a suitable geometry for the testing of multi-disciplinary optimization due to the description of the geometry by just a few parameters, see chapter 3.1.

In recent years, the high-fidelity calculations of reentry vehicle became state of the art. Also, the multi-disciplinary coupling of high-fidelity solvers were performed more frequently. However, these methods are in need of a high computational effort and create a massive amount of data. These facts make them less attractive for multi-disciplinary optimization due to the number of calculations needed. For this reason, low-fidelity solvers are needed within multi-disciplinary optimizations to reduce the parameter space for the high-fidelity optimizations. The low-fidelity solvers are much faster, but the accuracy of the results can highly lack validity dependent on the mission and geometry. Therefore, this paper gives insight into the differences between the high-, and low-fidelity multi-disciplinary solution for a generic HLRV.

2. Reference Data

The reference data for the comparison are high-fidelity coupled calculations, performed by Franze [3], along the generic trajectory depicted in the figure 1. The initial point $t = 0$ of the trajectory describes the separation from the motor at an altitude of $h = 85$ km with a Mach number of $M = 12.3$. The vehicle flies a dipping reentry until $t = 132$ s followed by pitching up and starting the cruise phase at $t = 200$ s. The high-fidelity solution is derived by the loose coupling of the DLR CFD solver TAU and the commercial CSM solver ANSYS. Within the coupling, the path of the trajectory is followed by a forced motion of the vehicle. The atmospheric conditions are defined by the ICAO standard atmosphere. The geometry calculated is slightly different in comparison to the geometry used in this paper. This is due to the limitation of the low-fidelity solvers for sharp edged configurations. The sharp leading edge is blunted by a radius of $r_{LE} = 4.5$ mm to create a more realistic geometry. Otherwise, the nose would burn blunt due to the high heat loads. The initial temperature of the structure at $t = 0$ is $T_w = 186.65$ K.

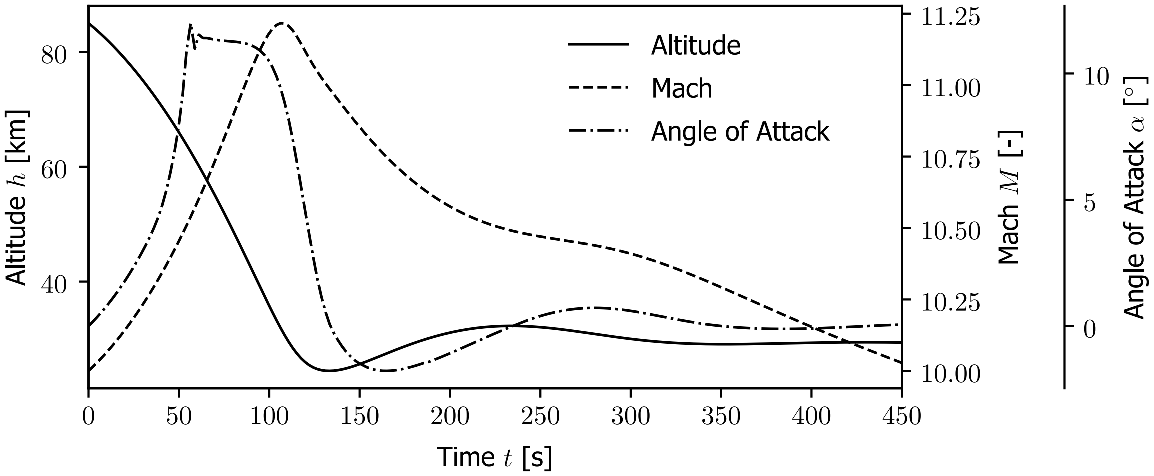

Fig 1. The generic trajectory used for the investigation.

3. Computational Setup

The computation is performed in the FlowSimulator [4] framework which is a simulation environment developed by the DLR. The environment enables to perform high-performance computations due to its foundation, the FSDataManager. The FSDataManager keeps all data needed for the simulation in RAM and manages the partitioned data in parallel computations. Thus, only files written on disc are for restart or the final results. Within the FlowSimulator, all tools are controlled by a Python layer which allows fast setup of simulations. Herein, the CoNF^{2}aS^2 module serves as a control program for multi-disciplinary simulations. The module provides simulation parameter for every solver, initiates the solvers, runs the calculations and governs the exchange of data between the solvers. The low-fidelity solvers, described in the following sections, are loosely coupled. The exchange of data between the solvers is performed with a time step of $\Delta t = 0.5\,$s. The CFD and CSM solver use the same surface mesh and use a cell-centered discretization. Thus, no interpolation of data is needed.

3.1. Geometry

The geometry used for the comparison is a HLRV. More precisely, a waverider geometry generated by the Osculating-Cone-Method [6] with a design Mach number of $M = 10$, see figure 2. The Osculating-Cone-Method generates a 3D flow field out of multiple 2D flow fields. The inviscid 2D flow field of the cone is calculated by the Taylor-Maccoll-Equation. The equation solves the characteristics of constant semi-vertical angles to describe the flow behind the shock generated by the cone. The semi-vertical shock angle is $\theta_s = 10°$.

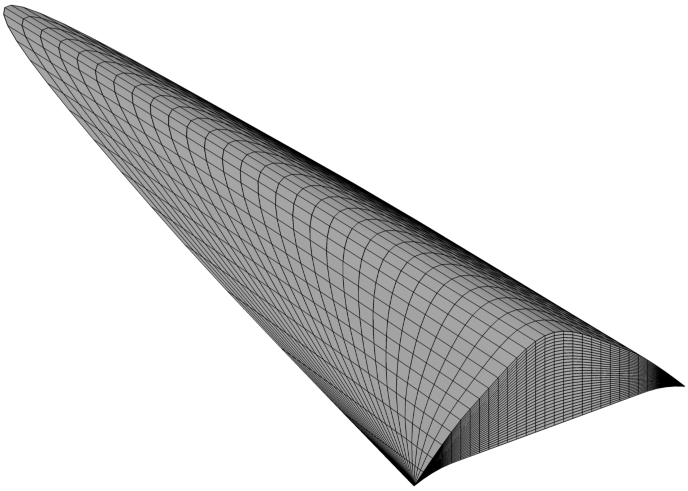

Fig 2. The generic waverider geometry.

The definition of the 3D flow field needs the description of the shock line. This line lies on a plane with the surface normal direction in the direction of the free stream flow. The shock line for the waverider, analyzed in this study, is described by a circle with the radius of $R = 2.3$, see figure 3. Thus, the 2D flow field is scaled by the radius and tilted with respect to the normal of every position on the circle. Consequently, a 3D cone flow field is formed. The trailing edge is defined by the luv-line. Here, the line is represented by a constant line towards $70\,\%$ of the half wingspan. Thereafter, the line is described by a quadratic function. Simultaneously, the luv-line is the starting point for the computation of the luv-surface. Beginning at this line, the stream lines are integrated upstream until the compression shock is reached. The intersection with the shock is the leading edge of the vehicle. The lee-surface is formed as a free stream surface, a surface parallel to the free stream. This results in a flow field without shocks nor expansions for the assumption of an inviscid flow. The sharp leading edge separates the luv- and lee-flow. Thus, the high pressure of the compression shock is trapped on the luv-side of the vehicle. The high lift to drag ration of the WR vehicle is based on this effect.

3.2. Aerodynamic

The program used for the aerodynamic calculation is a Python reimplementation of the Fortran HOT-SOSE [5] solver with the name FSSose. The evaluation of the pressure and friction on the configurations surface is performed by applying the Shock-Expansion-Method [1] and solutions of the boundary layer equation. The Shock-Expansion-Method is a local panel method which means only the local flow state and surface properties are taken into account for the calculation. Thus, an initial solution is calculated on the leading edge of the vehicle. Therefore, the oblique shock relations from freestream are conducted.

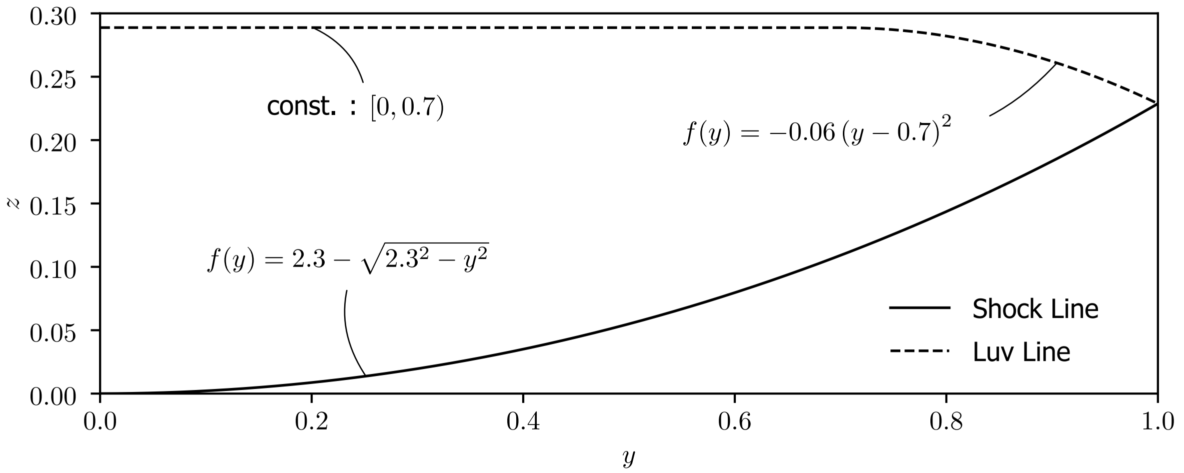

Fig 3. The lines to define the geometry of the WR.

Continuing with the initial condition, the Prandtl-Meyer-Expansion is applied w.r.t. the local deflection of the panels. This means, the path of the streamline is pre-defined by the structured surface mesh. If the local deflection angle is positive, the oblique shock relations are used. Herewith, the state of the perfect gas is calculated for every surface panel.

Furthermore, the skin friction is computed by the solution of the incompressible boundary layer equation. The Eckert-Reference-Enthalpy-Method [1] is used to take the compressibility effects into account

$$\frac{T^*}{T_e} = 1 + 0.032M_e^2 + 0.58\left(\frac{T_w}{T_e} - 1\right). \tag{1}$$

Therefore, the reference temperature T^* is evaluated w.r.t. the temperature T_e and Mach number M_e at the boundary layer edge as well as the temperature of the surface T_w. The edge state is taken from the Shock-Expansion solution. For the skin friction of the laminar flow, the Blasius solution [1] is conducted

$$c_{f,\text{lam}} = \frac{0.664}{\sqrt{Re_x^*}}. \tag{2}$$

In the Equation, the Reynolds number is evaluated at the current downstream position from the leading edge for the state of the reference temperature. The equation by Schlichting [2] is solved for the turbulent flow

$$c_{f,\text{turb}} = \frac{0.02296}{\left(Re_x^*\right)^{0.139}}. \tag{3}$$

Moreover, the transition of the boundary layer from laminar to turbulent flow is included by the relation given by Bowcutt [2].

$$\log_{10}\left(Re_{x_t}\right) = 6.421\,\text{exp}\left(1.209 \cdot 10^{-4} M_e^{2.641}\right) \tag{4}$$

The relation is based on the correlated data from sharp cone flows and blunt swept wings in supersonic flow.

3.3. Aerothermodynamic

The aerothermodynamic calculation is a module within the FSSose solver. The heat flux is evaluated by the Reynolds analogy [1]

$$C_H = \frac{c_f}{2s}. \tag{5}$$

The analogy describes the heat transfer for a flat plate by the skin friction and the Reynolds analogy factor s. The following factor is used

$$s = \left(Pr^*\right)^{\frac{2}{3}}. \tag{6}$$

Herein, the Prandtl number Pr^* is evaluated for the flow state evaluated by the Eckert-Reference-Enthalpy-Method.

3.4. Structure

The low-fidelity heating of the structure is described by a finite element 1D heat conduction solver. Hereby, the heat conduction equation is solved for every surface element in its normal direction into the structure. The outer surface boundary condition is set to the heat flux derived by the aerothermodynamic solver and a radiation model. The radiation is described by the Grey-Body-Radiation model

$$\dot{q}_r = \varepsilon\sigma(T_w^4 - T_\infty^4). \tag{7}$$

Herein, the emissivity ε is set to the value of the outer material. The Stefan-Boltzmann constant is σ, T_w the wall temperature and T_∞ the free stream temperature from the atmospheric model. The inner hull boundary condition is set to an adiabatic wall to keep the heat in the structure. This leads to a more conservative approximation due to the missing heat capacity of e.g. payload.
The structure itself is defined by a stack of three materials, an outer ceramic, an isolation and the structure material (aluminum). The material properties are listed in the table 1. The ceramic material is anisotropic which results in the given range of thermal conductivity. The conductivity in surface normal direction is the lowest value whereas the in-plane conductivity is defined by the highest value. For this low-fidelity structure model the low conductivity is taken into account only.

Table 1. The parameter of the material of the structure.

Material	**Thermal Conductivity** λ [Wm^{-1}K^{-1}]	**Isobaric Heat Capacity** [Jkg^{-1}K^{-1}]	**Density** [kgm^{-3}]	**Emissivity** ε [-]
Ceramic	12.5 to 125.0	1550.0	1900.0	0.8
Isolation	0.126	0.21	961.11	-
Aluminum	145.0	862.0	2800.0	-

The thickness of the material is defined by a simplified model. Therefore, the outlines of the structure are projected onto the x-y-plane, see the figure 4. Herein, the normal distance from the leading edge line to the cell center d is used as variable for the analytical functions describing the thickness. Furthermore, the distances to the projected lines are used change the functions, namely the distance from the leading edge line to the isolation d_I, to the inner structure d_S, to the inner hull d_H.

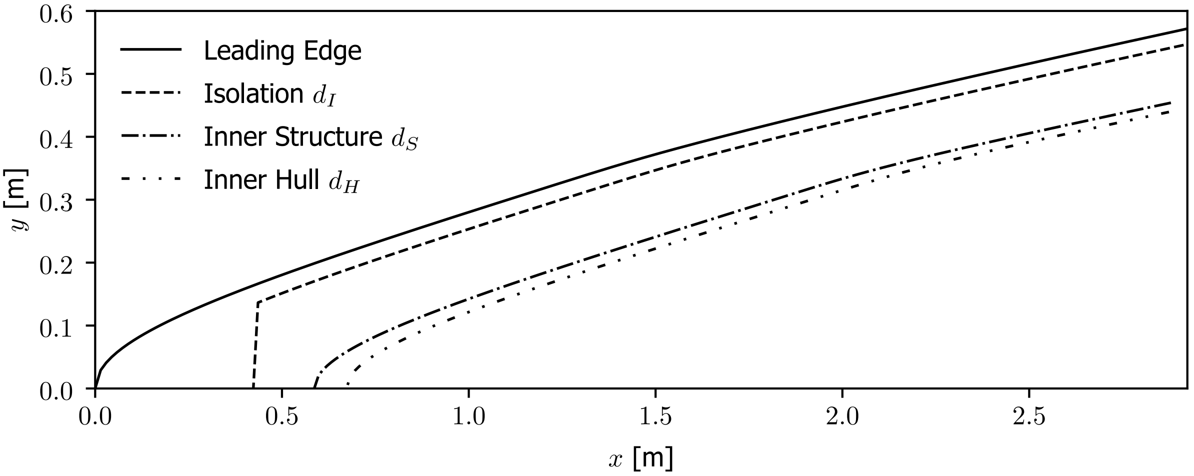

Fig 4. The projection of the structure onto the x-y-plane.

In general, the material thickness increases until a constant thickness is reached. This is due to the sharp leading edge of the WR. The ceramic thickness ψ_C is described by the equation 8. Hierin, the nose region needs special treatment to be filled towards the position of $x = 0.42335\,\text{m}$ which leads to a maximum thickness of $t_{\psi,\text{max}} = 0.018\,\text{m}$.

$$\psi_C(d) = \begin{cases} \dfrac{d}{3}, & \text{if } d < 0.03 \text{ and } x <= 0.42335 \\ \dfrac{4}{75}(d - 0.03) + 0.01, & \text{if } d >= 0.03 \text{ and } x <= 0.42335 \\ \dfrac{0.01d}{d_I}, & \text{if } d < d_I \text{ and } x > 0.42335 \\ 0.01, & \text{otherwise} \end{cases} \tag{8}$$

The thickness of the isolation ψ_I is defined with equation 9, the thickness of the inner structure ψ_S by equation 10, respectively.

$$\psi_I(d) = \begin{cases} \dfrac{0.03\,(d - d_I)}{d_S - d_I}, & \text{if } d_I <= d < d_S \\ 0.03, & \text{if } d >= d_S \\ 0, & \text{otherwise} \end{cases} \tag{9}$$

$$\psi_S(d) = \begin{cases} \dfrac{0.005\,(d - d_S)}{d_H - d_S}, & \text{if } d_S < d < d_H \\ 0.005, & \text{if } d >= d_H \\ 0, & \text{otherwise} \end{cases} \tag{10}$$

4. Results

The comparison of the calculations is conducted at three characteristic positions of the flight along the trajectory, at $t = 40\,\text{s}$, $t = 120\,\text{s}$ and $t = 200\,\text{s}$ of flight. The flow properties and flight attitude of the vehicle are listed in the table 2. Therewith, different conditions are taken into account. At the first position, the vehicle is at the beginning of the dipping maneuver. The structure is cold, and the density is low and the angle of attack is moderate. The second position is near the end of the reentry phase. Here, the heat load is high due to the high velocity and high angle of attack in low altitude. The last position is the beginning of the cruise phase which the vehicle should keep for a longer time. On this position, the vehicle is hot, radiates heat and cools down.

Table 2. The flow conditions for the characteristic points on the trajectory.

Time t [s]	**Altitude** h [km]	**Mach Number** M_∞ [-]	**AoA** α [°]	**Temperature** T_∞ [K]	**Density** ρ_∞ [kgm^{-3}]
40	70.8	10.34	4.6	215.29	$6.640075 \cdot 10^{-5}$
120	25.9	11.12	4.5	222.59	$3.401515 \cdot 10^{-2}$
200	31.1	10.58	-1.1	227.76	$1.517815 \cdot 10^{-2}$

4.1. Comparison

The comparison of the low- and high-fidelity data is performed by slices of constant y-coordinate. Three positions are studied, at $y = 0$, $y = \frac{b_H}{3}$ and $y = \frac{2b_H}{3}$ which are related to the half wingspan $b_H = 0.57\,\text{m}$. In the figure 5, the heat flux is depicted for the surface slices and the different times of flight along the trajectory within the coupled simulations. The solid lines describe the reference high-fidelity solution and the dashed lines the low-fidelity results. For a time of flight $t = 40\,\text{s}$, it can be seen, the heat flux is underestimated by the low-fidelity solver for all positions on the surface. The Reynolds number is low due to the low density at this position on the trajectory. Therewith, the critical Reynolds number for the turbulent transition is not reached for the whole configuration and the flow is stated as laminar flow. For the slice at $y = 0$, the maximum heat flux calculated by the high-fidelity is $\dot{q}_{\text{max}} = 0.71\,\text{MWm}^{-2}$ whereas the low-fidelity solution results in $\dot{q}_{\text{max}} = 0.03\,\text{MWm}^{-2}$.

At $t = 120\,\text{s}$, the heat fluxes in the leading edge region are underestimated. Here, the solver estimates a laminar flow. The transition to a turbulent boundary layer is approximately $\Delta x \approx 0.25\,\text{m}$ behind the leading edge. At this position, the heat flux increases and leads to an overestimation of the heat flux for the luv-surface. In the y center plane, the heat flux rises to $\dot{q} = 2.28\,\text{MWm}^{-2}$. On this position, the high-fidelity solution is $\dot{q} = 0.71\,\text{MWm}^{-2}$. Furthermore, the heat flux increases more gradually after a dip behind the high heat flux of the nose. The heat flux of the low-fidelity solver decreases towards the trailing edge to $\dot{q} \approx 1.65\,\text{MWm}^{-2}$ where the high-fidelity solver calculates $\dot{q} \approx 0.9\,\text{MWm}^{-2}$. In contrast, the lee-surface shows reasonable agreement.

The heat fluxes for the time of flight $t = 200\,\text{s}$ change in the leading edge region qualitatively. This is due to the negative angle of attack. The low-fidelity solution shows nearly similar heat fluxes for the luv- and lee-surface until the position is reached where the flow is stated as turbulent. In the luv-surface rear region, the low-fidelity solution is $\dot{q} \approx 0.41\,\text{MWm}^{-2}$ and the one of the high-fidelity solver is $\dot{q} \approx 0.2\,\text{MWm}^{-2}$.

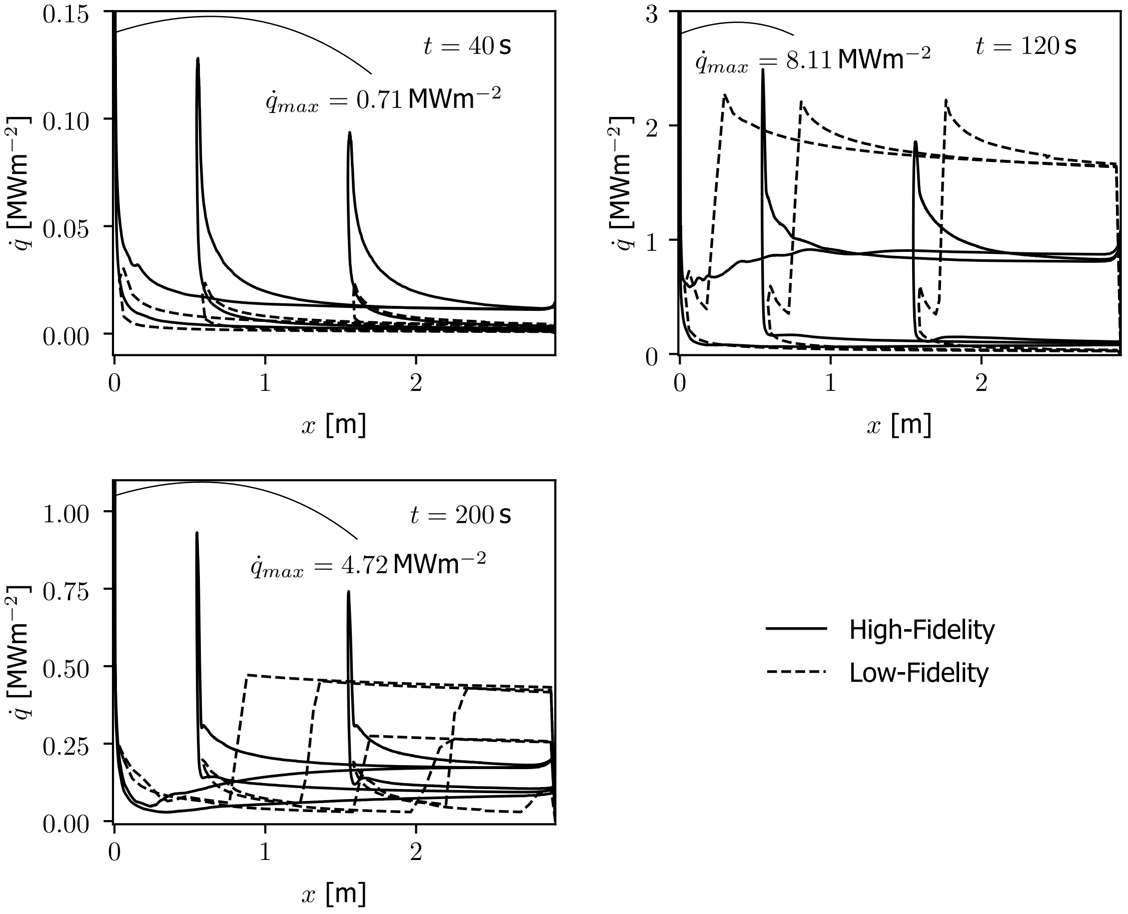

Fig 5. The heat flux $\dot{q}$ for constant y slices in the center plane, at $y = \frac{b_H}{3}$ and $y = \frac{2b_H}{3}$ for three positions on the trajectory.

The major difference of the leading edge heat fluxes can be described by the geometrical difference. The blunt leading edge results in a detached shock. Thus, the flow temperature is higher and so the heat flux. In contrast, the low-fidelity solver calculates an attached shock. The stagnation point is not taken into account. Furthermore, the first discrete value is calculated at the first surface element center position, which again is a few centimeters downstream.

The figure 6 displays the surface temperature distribution on the WR at the three characteristic positions on the trajectory, resulting from the coupled simulations. At $t = 40\,\text{s}$ the temperature of the surface is underestimated by the low-fidelity solvers. The reason is the underestimation of the heat fluxes as described above. The maximum temperatures in the slice at $y = 0$ are $T_{w,\text{max}} = 612.68\,\text{K}$ for the high-fidelity solver and $T_{w,\text{max}} = 213.28\,\text{K}$ for the low-fidelity solver.
The calculated temperatures on the luv-surface of the vehicle show a reasonable agreement between the two solutions for a time of flight of $t = 120\,\text{s}$. The discrepancy is approximately $\Delta T_w \approx 200\,\text{K}$. Differences can be seen in the region of $\Delta x \approx 0.5\,\text{m}$ from the leading edge. Here, the low heat fluxes from the low-fidelity solver result in low temperatures in this section of the vehicle. The peaks of the heat flux after the transition to a turbulent boundary layer are smoothed by the conduction into the structure.
For the time of flight $t = 200\,\text{s}$, the temperature in the nose region increases for the low-fidelity solution. Whereas, the high-fidelity solution shows a reduction of temperature. Furthermore, a temperature peak forms at $x = 0.35\,\text{m}$ with $T_w = 2468.88\,\text{K}$ for the low-fidelity solution. This temperature hotspot is the result of an element which is fully heated. Due to the adiabatic wall, as inner boundary condition, the element can not transfer heat into the inner hull. Consequently, the outer surface temperature quickly rises if the thermal capacity is filled. The phenomenon is damped in the 3D-high-fidelity calculation due to the in-plane heat exchange of the elements.

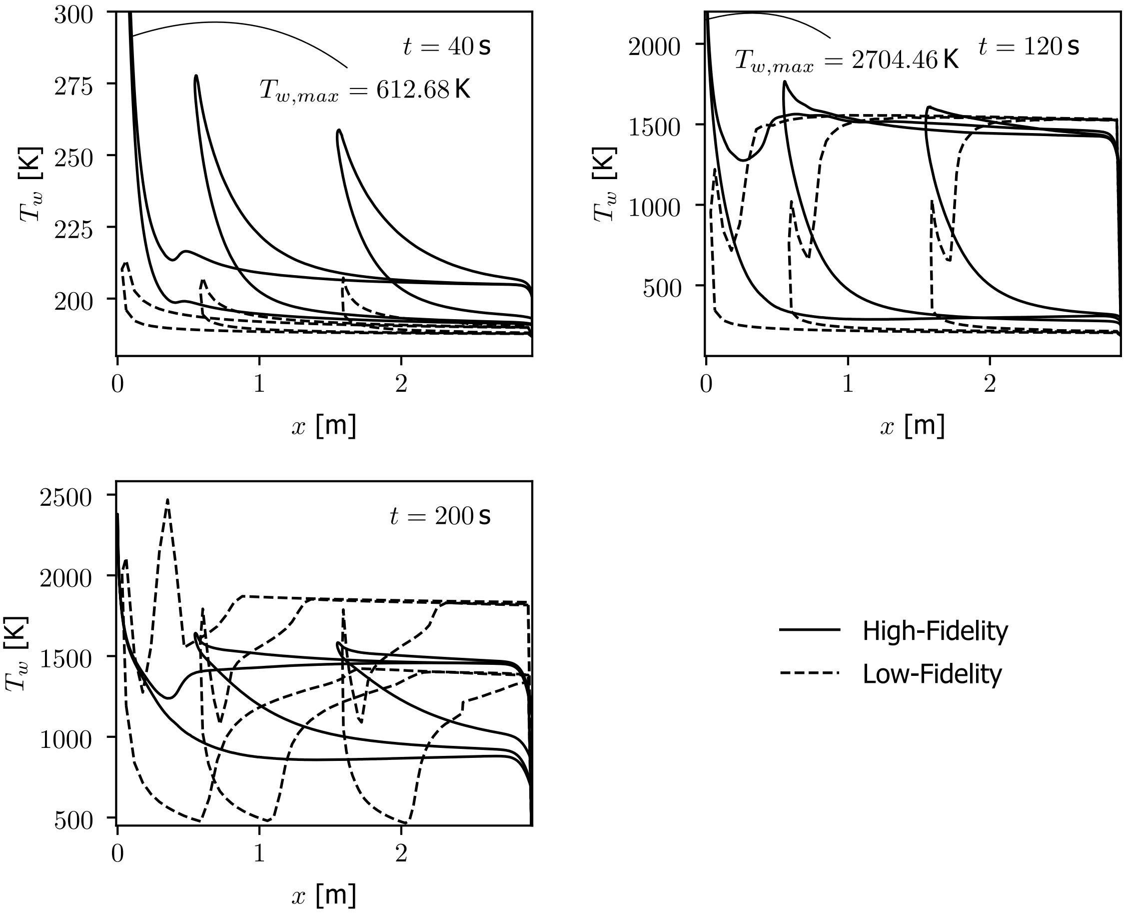

Fig 6. The surface temperature T_w for constant y slices in the center plane, at $y = \frac{b_H}{3}$ and $y = \frac{2b_H}{3}$ for three positions on the trajectory.

4.2. Influence of the Aerothermodynamic Model

The prediction of the turbulent transition is a problem which is influenced by a lot of parameters. Thus, the used empirical model brings uncertainty. For this reason, the influence of the transition is analyzed by comparison with calculations where a laminar or turbulent boundary layer is assumed for the whole trajectory. The resulting surface temperatures are illustrated in the figure 7 for $t = 120\,$s. It can be seen, the laminar theory highly underestimates the heating of the structure. The turbulent theory estimates the heating for the region downstream of the position $x = 0.5\,$m with reasonable agreement to the high-fidelity calculations. However, the reduction of the temperature behind the leading edge region is not recognized. The combination of both theories with the transition model shows this detail qualitatively. However, it has to be noted that the high-fidelity solution is generated with fully turbulent calculations. Consequently, the temperature reduction, before $x = 0.5$, is more likely due to the characteristics of the full ceramic nose of the 3D heat conduction. In the 3D calculation, the heat can be conducted to the lee-surface and in-plane. Thus, the effective heat capacity is higher than the capacity of the low-fidelity solver where only half the nose thickness is assigned to the luv-surface.

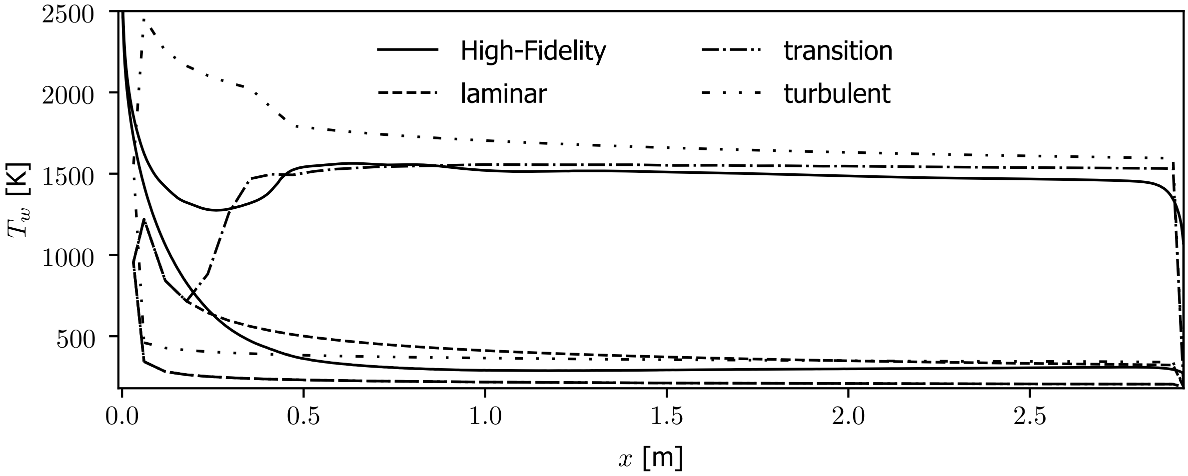

Fig 7. The surface temperature for different aerothermodynamic models at $t = 120\,$s for the surface slice with constant $y = 0$.

4.3. Influence of the Thermal Conductivity

The 1D conduction model used for the present analysis lacks the conduction of heat in the in-plane direction. This limits the modelling of the WR outer ceramic material. Thus, the high anisotrop material is described with one thermal conductivity in surface normal direction. Therefore, the true conductivity in normal direction, the mean value of both conductivities and the in-plane conductivity are compared. The resulting surface temperatures for the time of flight $t = 120\,$s are plotted in the figure 8. The best agreement with the high-fidelity coupled simulations is archived with the real thermal conductivity in normal direction. The higher the conductivity, the lower is the surface temperature. This is mostly evident where a second and third material is underneath the ceramic. The reason is the fast conduction of the introduced heat through the ceramic layer into the next. Consequently, the outer temperature is lower. In the leading edge region, the temperature differences are small for different thermal conductivities.

5. Conclusion

The paper compares the solution of a low-fidelity CFD/CSM-coupled simulation with the high-fidelity solution for a forced flight along a given trajectory. At characteristic positions along the trajectory, surface temperatures and heat fluxes are analyzed. The heat fluxes and temperatures are underestimated by the low-fidelity solver in high altitudes. For the position near the end of the reentry at $t = 120\,$s, the surface temperatures are in good agreement in some distance of the leading edge. The temperatures are

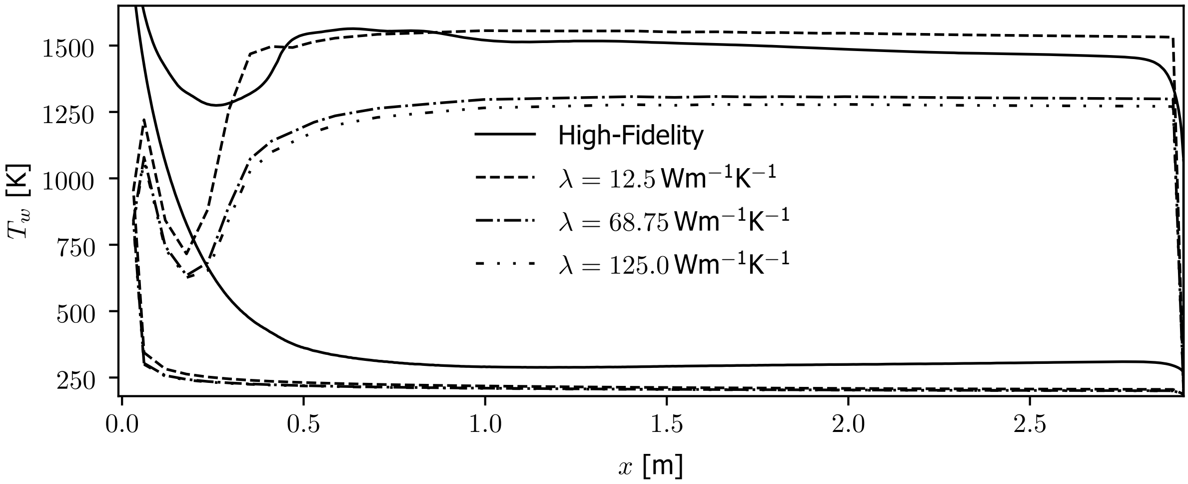

Fig 8. The surface temperature for different thermal conductivities at $t = 120\,\text{s}$ for the surface slice with constant $y = 0$.

overestimated at the beginning of the cruise phase. The comparison of the aerothermodynamic models shows good results for the laminar/turbulent transition model and for the turbulent model behind the solid ceramic nose. Furthermore, the real normal conductivity of the ceramic material shows the best results, despite its high anisotropie.

Some drawbacks of the solver are shown. The implemented low-fidelity flow solver leads to best results for flat plates. Hence, the leading edge heating is underestimated in regard to the high-fidelity calculation for the blunt nose vehicle. The calculation along the trajectory is an integration of heat fluxes. This leads to an accumulation of errors. Thus, the low-fidelity coupled solution is more sensitive due to higher errors of the single solution. Moreover, the one-dimensional heat conduction is not sufficient for highly anisotropic material properties due to the missing in-plane conduction. Further, the filled noses shows an underestimation of the heat capacity.

In the future, methods will be included in the existing software to account the mentioned drawbacks. The geometric difference can be minimized by low-fidelity models to calculate blunt leading edges like the Fay-Riddell method [1] for the heat flux at the stagnation point. Furthermore, an extended model for filled noses can be used to better approximate the heat capacity of the nose.

Therewith, multi-fidelity methods can be utilized for the design, fast analysis and optimization of reentry geometries over the whole trajectory. Furthermore, the multi-fidelity methods can be empowered with methods of artificial intelligence and machine learning to lift the process to a new level.

References

[1] Anderson, J.: Hypersonic and High-Temperature Gas Dynamics, Second Edition, American Institute of Aeronautics and Astronautics, Inc., 2006

[2] Bowcutt, K., Anderson, J., Capriotti, D.: Viscous Optimized Hypersonic Waveriders, 25th AIAA Aerospace Sciences Meeting, 1987

[3] Franze, M., Barz, F.: Comparison of Models for Aerothermal Load Prediction using Coupled Trajectory Simulations of a High Lift Reentry Vehicle, HiSST: 3rd International Conference on High-Speed Vehicle Science Technology, Busan, Korea, 2024

[4] Meinel, M., Einarsson, G.: The FlowSimulator Framework for Massively Parallel CFD Applications, PARA, Reykjavik, Island, 2010

[5] Reisch, U., Streit, T.: Surface Inclination and Heat Transfer Methods for Reacting Hypersonic Flow in Thermochemical Equilibrium, New Results in Numerical and Experimental Fluid Mechanics: Contributions to the 10th AG STAB/DGLR Symposium Braunschweig, Germany, 1996

[6] Sobieczky, H., Dougherty, FC. and Jones, K.: Hypersonic Waverider Design From Given Shock Waves, Proceedings of the First International Hypersonic Waverider Symposium, University of Maryland College Park, MD, 1990